Research Article | Vol. 29, No. 8 / 12 April 2021 / Optics Express 12429
Optics EXPRESS

Microsphere kinematics from the polarization of tightly focused nonseparable light

STEFAN BERG-JOHANSEN,[1,2] MARTIN NEUGEBAUER,[1,2] ANDREA AIELLO,[1] GERD LEUCHS,[1,2] PETER BANZER,[1,2,3] AND CHRISTOPH MARQUARDT[1,2,*]

[1]Max Planck Institute for the Science of Light, Staudtstr. 2, D- 91058 Erlangen, Germany
[2]Institute of Optics, Information and Photonics, University Erlangen-Nuremberg, Staudtstr. 7/B2, D- 91058 Erlangen, Germany
[3]Institute of Physics, University of Graz, NAWI Graz, Universitätsplatz 5, 8010 Graz, Austria
*christoph.marquardt@mpl.mpg.de

Abstract: Recently, it was shown that vector beams can be utilized for fast kinematic sensing via measurements of their global polarization state [Optica **2**, 864 (2015)]. The method relies on correlations between the spatial and polarization degrees of freedom of the illuminating field which result from its nonseparable mode structure. Here, we extend the method to the nonparaxial regime. We study experimentally and theoretically the far-field polarization state generated by the scattering of a dielectric microsphere in a tightly focused vector beam as a function of the particle position. Using polarization measurements only, we demonstrate position sensing of a Mie particle in three dimensions. Our work extends the concept of back focal plane interferometry and highlights the potential of polarization analysis in optical tweezers employing structured light.

1. Introduction

Optical beams with a nonseparable mode structure [1,2] have recently garnered attention in a wide range of subfields in optics, including generalized optical coherence theory [3], simulations of quantum algorithms [4], quantum channel characterization and correction [5], diffraction-free beam propagation [6], broad-band cavity design [7], and metrology [8]. In this context, vectorial structured light plays a major role [9]. The nonseparability occurring between polarization and spatial degrees of vector beams was recently utilized for fast kinematic sensing based on polarization measurements [10].

In the present work, we extend the idea of position sensing with nonseparable modes to the nonparaxial regime, relevant to optical tweezers [11,12] and nano-optics [13–16]. In this regime, Gauss's law $\nabla \cdot \mathbf{E} = 0$ couples different polarization components of laterally bounded fields, leading to a complex polarization structure in the focal region even for fields which are homogeneously polarized in the paraxial approximation [17–21]. Both radially polarized beams [22–27] and polarization effects [28–31] have been studied in optical tweezers in the past, and existing approaches to 3D sensing include methods with multiple beams [32], imaging [33,34], and digital holography [35]. Of particular interest for the present work is the concept of back focal plane interferometry [36–42], where a particle-position-dependent phase delay between incoming and scattered field, due to the Gouy phase, is exploited for axial position sensing. In this approach, the lateral position is detected with a quadrant diode. A theoretical analysis of optimal position measurements of a dipole in a strongly focused field with polarization-insensitive detectors was recently given in [43].

Here, instead of spatially partitioning the field with a quadrant diode, we consider a partition in polarization space. First, we investigate the polarization state of forward scattered light from dielectric microspheres in the focal region of a tightly focused radially polarized beam

#419540 https://doi.org/10.1364/OE.419540
Journal © 2021 Received 11 Jan 2021; revised 17 Mar 2021; accepted 24 Mar 2021; published 7 Apr 2021

Optics EXPRESS

as a function of particle position. We find a strong correlation between particle position and far-field polarization state. Through numerical simulations, we show that the essential features of the observed polarization structure can be reproduced by an electric dipole model, and that a similar, albeit weaker, particle-position-dependent polarization structure arises also for a linearly polarized Gaussian beam, which has separable degrees of freedom in the paraxial approximation. We numerically compare the signals obtained from polarization measurements with those obtained from quadrant diode detection for the same system. Next, we demonstrate experimentally that three-dimensional position sensing of a particle moving in the focal region of a tightly focused radially polarized beam is feasible using polarization data only. Our results suggest that polarization analysis in optical tweezers, combined with structured input light, presents a promising complement to existing approaches.

2. Methods

2.1. Theory

The main principle of the investigated scheme is described in Fig. 1(a). It is equivalent to the experimental setting. An incoming tightly focused beam of light — wave fronts marked as gray lines — interacts with a dielectric micron-sized particle (small gray circle). The local field distribution of the beam at the particle position excites a mode inside the particle, scattering light into the far-field. This scattered light (red phase fronts) interferes with the transmitted beam, changing the overall far-field intensity and polarization of the diverging beam, depending on the position of the particle relative to the focus. We partially collect this far field with a microscope objective and measure its Stokes parameters with a detection system. Since the position of the particle is encoded in the intensity and polarization state of the transmitted light, we can infer the position of the particle relative to the beam using the measured Stokes parameters.

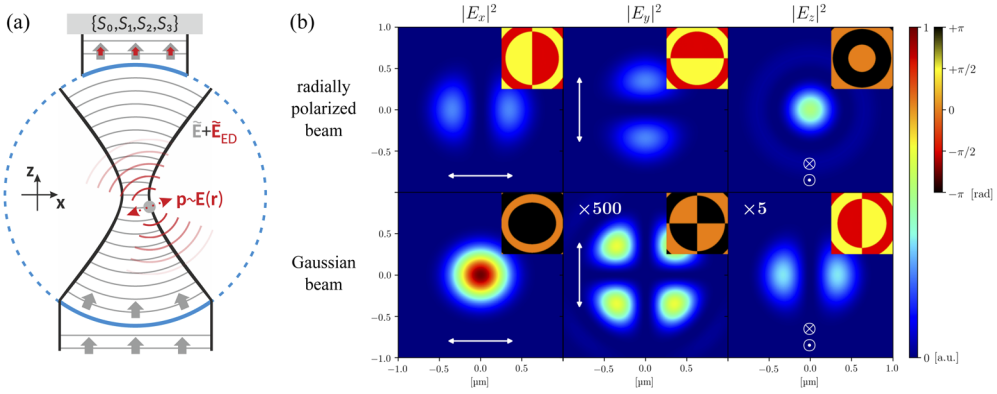

Fig. 1. (a) Experimental concept. A tightly focused beam excites a dielectric particle located in the focal region. The excited field is shown here as a linear electric dipole for simplicity, although for our beams it is in general a spinning dipole. The Stokes parameters of the electric field transmitted in the forward direction are measured as a function of the particle position. (b) Simulated electric energy density components in the focal plane of a tightly focused radially polarized beam (top) and an x-polarized Gaussian beam (bottom). The insets show the phase distribution for each component.

For an exemplary theoretical description of our concept, we first consider the incoming tightly focused monochromatic beam of light. The vectorial angular spectrum (VAS) of the beam $\tilde{\mathbf{E}}(k_x, k_y)$ — the VAS is defined with respect to the x-y-plane (focal plane with $z = 0$) — and the real space field distribution $\mathbf{E}(\mathbf{r})$ with $\mathbf{r} = (x, y, z)$, are linked by a vectorial Fourier transformation

Optics EXPRESS

[20],

$$\mathbf{E}(\mathbf{r}) = \iint \mathrm{d}k_x \mathrm{d}k_y \, \tilde{\mathbf{E}}(k_x, k_y) \exp(\imath \mathbf{k}\mathbf{r}). \tag{1}$$

All plane waves propagate in the positive z-direction (k_z>0). The theoretical electric field distribution in the focal plane for two beam types is shown in Fig. 1(b). The real space field distribution determines the interaction with the particle. For the sake of simplicity, we only consider the fundamental electric dipolar mode of the dielectric particle, neglecting all magnetic and higher order electric resonances. The excited electric dipole moment is proportional to the local electric field, $\mathbf{p}(\mathbf{r}_0) = \alpha_e \mathbf{E}(\mathbf{r}_0)$, with α_e being the electric polarizability of the particle and $\mathbf{r}_0$ its position. The particle-position-dependent emission of the excited electric dipole moment in the VAS representation reads [20]

$$\tilde{\mathbf{E}}_{ED}(k_x, k_y, \mathbf{r}_0) = [\mathbf{M}]\, \mathbf{E}(\mathbf{r}_0), \tag{2}$$

where

$$[\mathbf{M}] = \frac{\imath \alpha_e k^2 e^{\imath \mathbf{k}\mathbf{r}_0}}{8\pi\epsilon_0 k_z} \begin{pmatrix} 1 - \frac{k_x^2}{k_0^2} & -\frac{k_x k_y}{k_0^2} & -\frac{k_x k_z}{k_0^2} \\ -\frac{k_x k_y}{k_0^2} & 1 - \frac{k_y^2}{k_0^2} & -\frac{k_y k_z}{k_0^2} \\ -\frac{k_x k_z}{k_0^2} & -\frac{k_y k_z}{k_0^2} & 1 - \frac{k_z^2}{k_0^2} \end{pmatrix}.$$

The superposition of the VAS of the incoming beam with the VAS of the excited dipole moment results in the total VAS,

$$\tilde{\mathbf{E}}_T(k_x, k_y, \mathbf{r}_0) = \tilde{\mathbf{E}}_{ED}(k_x, k_y, \mathbf{r}_0) + \tilde{\mathbf{E}}(k_x, k_y). \tag{3}$$

As a next step, we take into account the detection geometry and calculate the total field distribution behind an aplanatic microscope objective with focal length f used for collecting the transmitted beam and the scattered light. The objective is confocally aligned with respect to the incoming tightly focused beam, implying that the field behind the objective is collimated (paraxial) with $E_T^z \approx 0$ as long as the particle is close to the focal plane ($z \ll f$). Using the formalism introduced in [17] to describe the rotation of the field vectors and the energy conservation at the reference sphere of the microscope objective, we arrive at the x- and y-components of the transmitted field,

$$\begin{pmatrix} E_x(k_x, k_y, \mathbf{r}_0) \\ E_y(k_x, k_y, \mathbf{r}_0) \end{pmatrix} \propto [\mathbf{R}]\, \tilde{\mathbf{E}}_T(k_x, k_y, \mathbf{r}_0), \tag{4}$$

where

$$[\mathbf{R}] = \sqrt{\frac{k_z}{k}} \begin{pmatrix} \frac{k_x^2 k_z}{k_\perp^2 k} + \frac{k_y^2}{k_\perp^2} & \frac{k_x k_y}{k_\perp^2}\left(\frac{k_z}{k} - 1\right) & -\frac{k_x}{k} \\ \frac{k_x k_y}{k_\perp^2}\left(\frac{k_z}{k} - 1\right) & \frac{k_x^2}{k_\perp^2} + \frac{k_y^2 k_z}{k_\perp^2 k} & -\frac{k_y}{k} \end{pmatrix}.$$

Finally, we calculate the local Stokes parameters defined by: $S_0 = |E_x|^2 + |E_y|^2$, $S_1 = |E_x|^2 - |E_y|^2$, $S_2 = 2\,\mathrm{Re}\, E_x E_y^*$ and $S_3 = -2\,\mathrm{Im}\, E_x E_y^*$. An integration over the full back focal plane of the collecting objective results in the particle-position-dependent global Stokes vector $\mathbf{S}(\mathbf{r}_0)$. Throughout this paper, we use a unitless convention whereby $s_0(\mathbf{r}_0)$ represents the integrated intensity normalized to the background value (i.e. without a particle), while $s_1, s_2, s_3(\mathbf{r}_0)$ are normalized to the local intensity. The position dependence of $\mathbf{s}(\mathbf{r}_0)$ is one of the main results of the manuscript.

Optics EXPRESS

2.2. Simulation

Based on the theoretical model described in Sec. 2.1, a numerical simulation of the far-field Stokes vector $\mathbf{s}(\mathbf{r}_0)$ was carried out for both a radially polarized beam and a linearly polarized Gaussian beam. The initial VAS was computed numerically with a custom MATLAB program implementing the vectorial diffraction theory due to Debye [44], Richards and Wolf [17] for the respective paraxial input fields with 200 plane wave components.

Figure 2 shows the simulated position-dependent global polarization state in the far field for two types of input fields, a radially polarized beam and a linearly polarized Gaussian beam. For both beams, the on-axis s_0 values display a positive gradient as the particle moves through focus in the $+z$-direction. This is a known effect which can be intuitively understood by considering the Gouy phase shift incurred by the incoming field [36–42] (it should be noted that the NA of the detection path is smaller than the NA of the incoming path). Depending on the axial particle position, the phase relation – in the far field – between incoming field and the dipole field leads to destructive or constructive interference. The same principle also causes a lateral gradient. This, too, is inverted as the particle passes through focus in the axial direction.

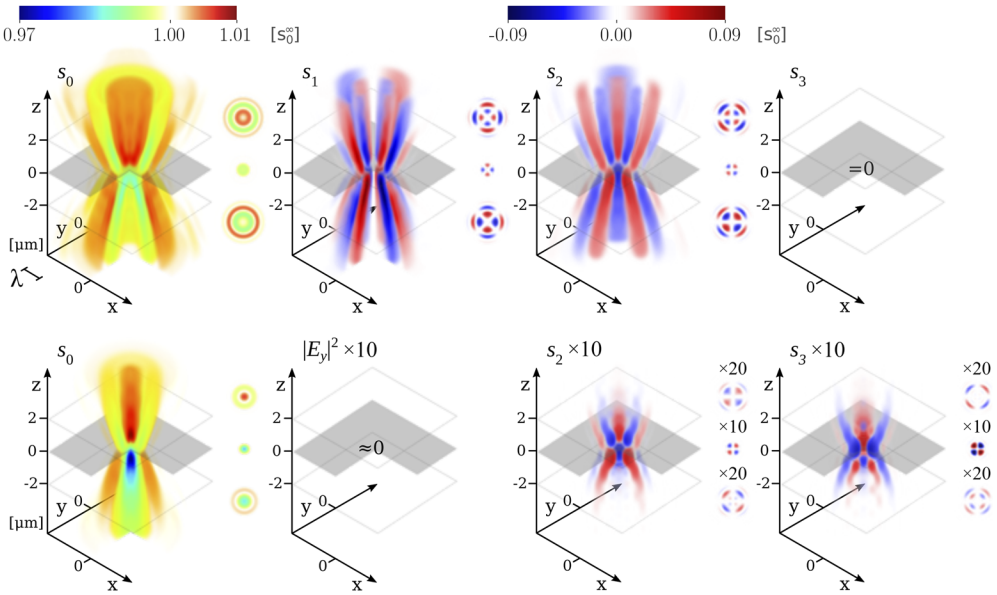

Fig. 2. Numerical simulation of the global polarization state in the far-field as a function of the position of a ∅ 2 µm (= 1.88 λ, n = 2.6) particle in the focal region of a radially polarized beam (top) and a linearly polarized Gaussian beam (bottom), with focusing NA 0.87 and collection NA 0.22. Note that the axes indiate particle position (i.e., this figure does not show a spatial field distribution). s_0 (intensity) is normalised to the background value (without a particle), while s_1, s_2, s_3 are normalised to the corresponding value of s_0 at each coordinate. For the Gaussian beam, the y-polarized intensity component $|E_y|^2$ is shown in place of s_1, as this Stokes parameter is dominated by the x-polarized input state. For clarity, background values are rendered transparently, and the front quadrant is cut out to reveal a cross-section of the axial values (missing values can be inferred from symmetry). Each panel spans a volume of $6 \times 6 \times 10\,\mu\text{m}^3$. The focal plane at $z = 0$ is indicated in grey. Insets to the right of each volume show transverse cross-sections at $\{\pm 2; 0\}$ µm. Multiplicative numbers indicate gain applied for better visibility. See the text for discussion.

In Fig. 3, we compare the simulated signal for conventional quadrant diode detection with the simulated signal for polarization detection for a laterally displaced particle in the focal plane of a

Optics EXPRESS

tightly focused radially polarized beam. The signals are simulated for two particle refractive indices, one corresponding to the particles used in the experiment ($n = 2.6$) and one arbitrary lower value ($n = 1.7$). The polarization detection is sensitive to the particle's refractive index and yields higher values when the index is lower. This increase in sensitivity is observed in all planes, not just the focal plane shown in Fig. 3. By contrast, the quadrant detection is more sensitive to the collection NA, changing both amplitude and sign across the three simulated values 0.3, 0.6 and 0.9. This agrees with existing numerical and experimental results for Gaussian beams [37,39]. Polarization detection is hardly affected by the collection NA in the focal plane, but we observe that limiting the collection NA leads to larger signals outside of the focal plane. Consequently, there is a trade-off between the axial sensitivity and the size of the volume in which lateral displacements can be detected.

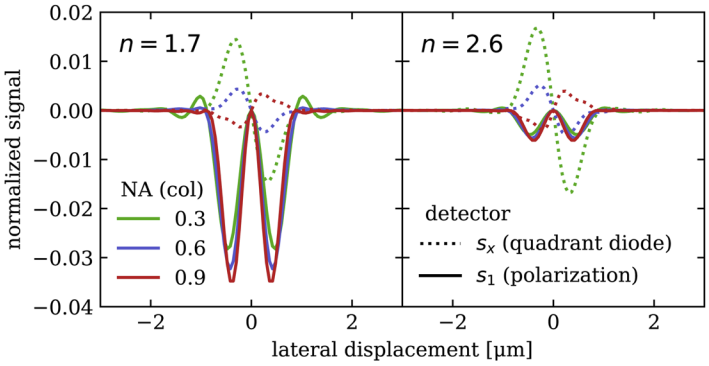

Fig. 3. Simulated response for the lateral displacement of a particle in the focal plane of a radially polarized beam for a quadrant diode measurement (dotted) and a polarization measurement (line), for selected particle refractive indices (left, right) and collection NAs (green, purple, red). The quadrant diode signal s_x represents the intensity difference between the right and left half-planes at the collection aperture. The remaining simulation parameters are chosen in accordance with the experiment (see Sec. 2.3).

In quadrant detection, the maximum gradient occurs on-axis, allowing for accurate measurement of small displacements about the origin. On the other hand, for a radially polarized beam the polarization detection's maximum gradient occurs off-axis, close to the zero gradient of the quadrant signal. This suggests that the linear range of lateral displacement measurements can be enhanced by including the polarization degree of freedom (note that quadrant- and polarization detection can, in principle, be performed simultaneously without optical losses).

We have seen that quadrant detection and polarization detection yield very different results for the same beam and particle. For polarization detection, the choice of input field also greatly affects the observable signals, as seen by comparing the radially polarized and Gaussian beams in Fig. 2. The optimal input field will ultimately depend on the application. For the problem of particle tracking, fields of the "full Poincaré" (FP) type [45] may be promising candidates, since they possess a one-to-one correspondence between polarization and transverse position in the paraxial approximation. A full exploration of different input fields is beyond the scope of this work. Here, we implement a proof-of-principle experiment using a radially polarized beam.

2.3. Experiment

A cw laser centered at $\lambda = 1064$ nm, emitting in a linearly polarized Gaussian mode, was passed through a liquid crystal mode converter followed by a Fourier filter to generate a radially polarized beam. The beam was focused with an aplanatic oil immersion objective (effective NA 0.9) onto single titania microspheres (TiO_2, $\varnothing$ 2 µm, $n \sim 2.5$) embedded in thiodiethanol (TDE, $n_m = 1.50$)

Optics EXPRESS

[46]. The typical optical power in the plane of the particle was 10 mW. The transmitted light was collimated by a second objective and directed to a beam splitter cascade for the detection of the individual Stokes parameters.

For free particle measurements, a single particle was trapped in the beam. We used the piezoelectric motion stage on which the probe was mounted to nudge the particle in different directions out of the trap while recording the Stokes parameters $\mathbf{s}(t)$. Reconstructing the trajectory from polarization data requires the particle-position-dependent Stokes vector $\mathbf{s}(\mathbf{r}_0)$, which we measured experimentally. Following a free measurement, we temporarily increased the trap stiffness by increasing the optical power to 40 mW and shifted the piezo stage in the $+z$-direction until the lower substrate made contact with the particle. This resulted in the particle becoming attached to the substrate, and its position perfectly correlated with the subsequent motion of the piezo stage. The particle was then scanned laterally across a plane centered on the beam axis. By repetition, the particle-position-dependent Stokes vector $\mathbf{s}(\mathbf{r}_0)$ was built up on a $6 \times 6 \times 10$ μm^3 volume. The trajectory was reconstructed using an algorithm conceptually equivalent to [10]. Further details on the experimental setup and the tracking algorithm can be found in Supplement 1.

3. Experimental results

3.1. Particle-position-dependent Stokes parameters

Figure 4 shows the experimentally recorded particle-position-dependent Stokes parameters s_0, s_1, s_2 for a 2 μm TiO_2 particle scanned through a radially polarized beam. The full set of 40 planes (spaced by 200 nm) is visualised in Fig. 5. The results reproduce the key features predicted by the simple theoretical model based on dipole scattering shown in Fig. 1(a) and Fig. 2, including the axial s_0-dependence, lateral dependence of s_1, s_2, and sign inversion relative to the focus. s_1 and s_2 are qualitatively identical up to a 45° rotation, as expected from the focal field distribution. When the particle is several Rayleigh ranges away from the focal plane, the parameters strongly resemble the polarization distribution of the paraxial mode, which agrees with intuition.

The polarization state of an ideal radially polarized beam in the paraxial regime is characterized by $s_3 = 0$ both locally and globally. The ideal global far-field polarization state is still $s_3 = 0$ when a particle is placed in the focal region, for any position of the particle. This is because any regions of locally circular polarization are cancelled in the global polarization state by another region of the opposite sign due to the symmetry of the ideal mode. The measured s_3 component (not shown) displayed an asymmetric nonzero pattern due to asymmetries in the prepared mode and potentially also due to a spatially inhomogeneous coupling in the detection plane. The pattern did not arise from the properties of individual particles because it was reproduced identically between scans of different particles. This allowed us to include the nonzero s_3 component in the map $\mathbf{s}(\mathbf{r}_0)$ used for position sensing.

3.2. Position sensing

Figure 6 shows the results for position sensing of a free TiO_2 particle placed in the focal region of a tightly focused radially polarized beam. In Panel 6(a), the particle is at equilibrium in the optical trap potential behind the focal plane. In Panels 6(b)–(e), the particle was nudged out of the trap by initiating a motion of the piezo stage supporting the medium in the $+x$-, $+y$-, $+z$-, and $-z$-directions, respectively. The trajectory shown was inferred based on the measured polarization data only, demonstrating motion detection in three dimensions from polarization-resolved measurements of forward-scattered structured light.

The measurement precision is affected by pointing instabilities (which we attempted to minimize with large active photodiode areas, ∅ 500 μm), as well as laser noise and detector noise.

Optics EXPRESS

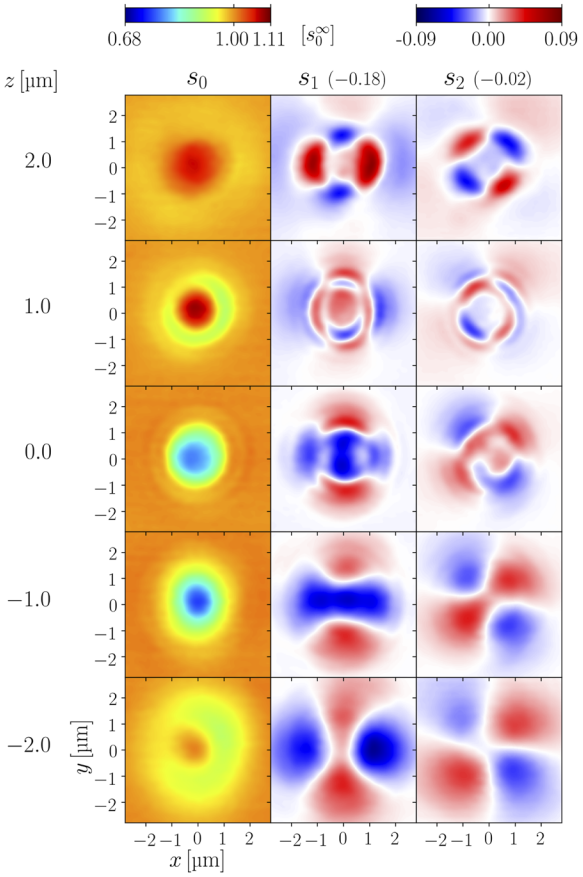

Fig. 4. Experimentally measured particle-position-dependent Stokes parameters $\{s_0, s_1, s_2\}(\mathbf{r}_0)$ in the far field for a ∅ 2 µm TiO_2 particle in the focal region of a tightly focused radially polarized beam. Offsets (indicated in parentheses) were applied uniformly to s_1 and s_2 to make their background values zero for clarity of presentation.

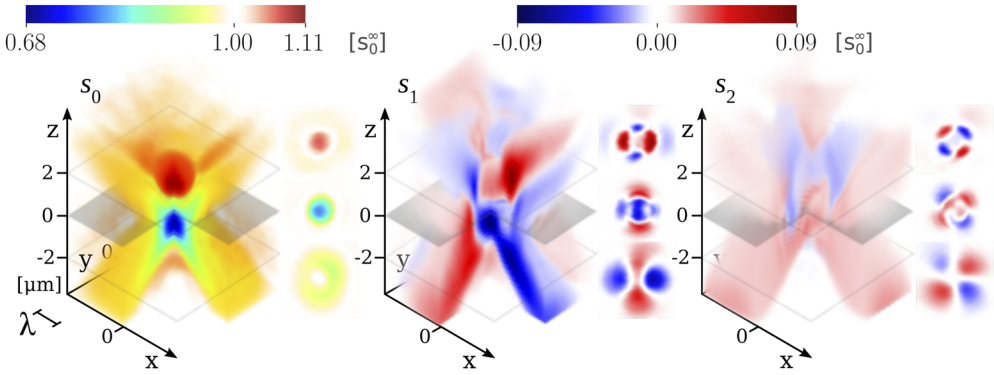

Fig. 5. The full dataset of Fig. 4 visualized for all 40 planes. As in Fig. 2, the front quadrant has been cut out for clarity. This makes s_1 appear more intense than s_2, but as shown by the insets, the components are approximately balanced.

Optics EXPRESS

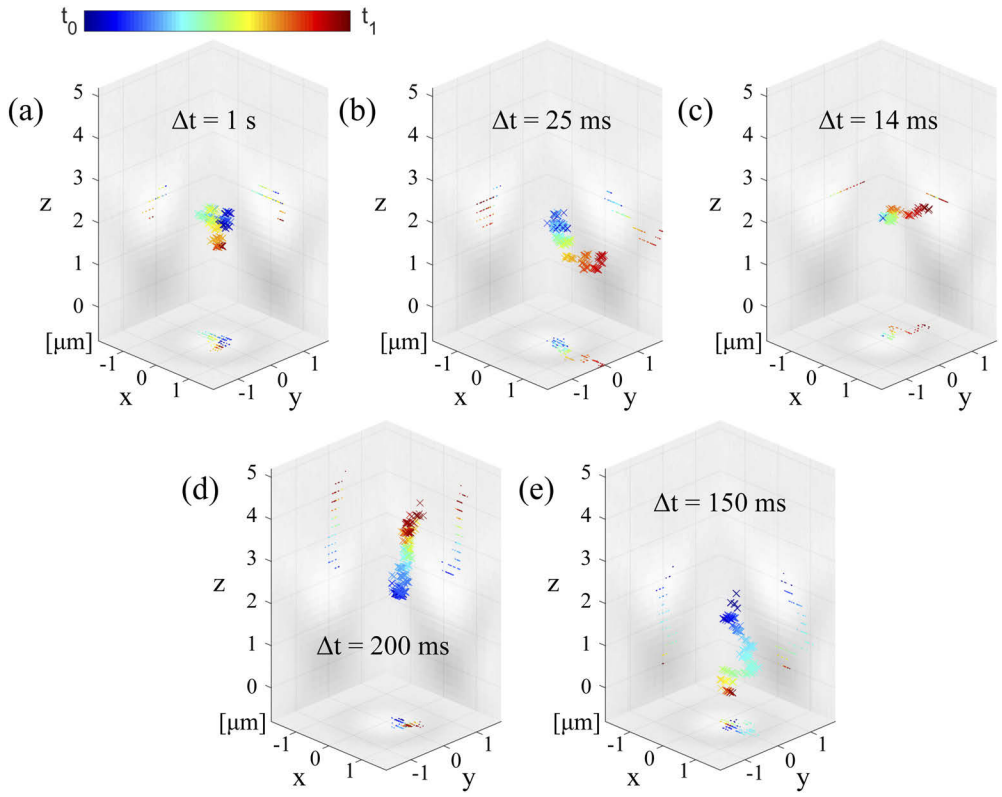

Fig. 6. Experimental results for three-dimensional position sensing of a TiO_2 microsphere in the focal region of a tightly focused radially polarized beam. In Panel **(a)**, the particle is undergoing Brownian motion in the trap potential, while in Panels **(b)**–**(e)** it is nudged in the $+x$-, $+y$-, $+z$-, and $-z$-directions, respectively. Motion is induced by moving the substrate supporting the medium in which the particle is suspended along the respective axes. Color indicates the time coordinate, normalized in each panel to match the duration of the measurement. The gray backdrops indicate the distribution of $s_0(\mathbf{r}_0)$ in the plane through the origin, similar to Fig. 5 (brighter backdrop corresponds to higher values of s_0).

These sources of error equally affect quadrant detectors. However, our computational approach means that our method is additionally affected by any mismatch between $\mathbf{s}(\mathbf{r}_0)$ (the calibration measurement) and $\mathbf{s}(t)$ (the free particle measurement). Such a mismatch can lead to distorted trajectories and adversely affects accuracy. In our prototype implementation, we frequently observed a mismatch caused by slow drifts occurring between calibration and measurement. We worked around this drift by recording the background value $\mathbf{s}(\mathbf{r}_0 \to \infty)$ over time, and calculated a linear correction factor for each measurement. This correction factor was applied to the measured Stokes vector $s_i(t)$ in post-processing, resulting in the trajectories shown in Fig. 6. While the inferred trajectories agree with the expected trajectories, it is not clear, for example, whether the curved trajectory in panel 6(e) is due to the actual physical trajectory or a mismatch artefact. Overcoming calibration table mismatch is crucial to improving the tracking accuracy with this method.

Optics EXPRESS

4. Conclusion

We have investigated the far-field particle-position-dependent global polarization state resulting from a dielectric microsphere placed in a tightly focused vector beam. A simple dipole scattering model was shown to reproduce the main qualitative features of the observed position-dependent polarization, providing insight into the underlying physical principle. Our work thus extends the idea of back focal plane interferometry to the polarization degree of freedom. Using this idea, we have demonstrated three-dimensional position sensing from polarization measurements without spatially resolving the scattered field. For this we calibrated our system for a specific combination of focal field and particle, and collected data traces for free particles which allowed the particle position to be obtained computationally.

Although all fields display some degree of polarization coupling when tightly focused, we have shown that paraxial vector beams lead to particularly large polarization gradients in the focal region compared to the more commonly used Gaussian beams, placing our work in the context of structured light with nonseparable degrees of freedom. Our numerical simulations indicate that polarization measurements, when combined with structured input light, can extend the transverse range of linearity of conventional quadrant diode detection schemes. It is therefore conceivable that polarization analysis combined with structured input light could complement quadrant diode detection in optical tweezers. Measurements of this kind could, for example, be realized by placing a quadrant diode in each output port of a polarizing beam splitter, and considering the differences between the total intensities as well as the individual quadrant signals. The approach can be extended to vector beams with other polarization patterns, such as azimuthally polarized beams, "spiral" beams, their counter-rotating versions, more exotic beams displaying nonzero net transverse angular momentum [47], full Poincaré beams [45], as well as different wavelength regimes, opening many interesting avenues for exploration.

Funding. H2020 Future and Emerging Technologies (732894 HOT, 829116 SuperPixels).

Acknowledgments. The authors thank Lucas Alber for suggesting thiodiethanol as mounting medium.

Disclosures. The authors declare no conflicts of interest.

Supplemental document. See Supplement 1 for supporting content.

References

1. R. J. Spreeuw, "A classical analogy of entanglement," Found. Phys. **28**(3), 361–374 (1998).
2. A. Aiello, F. Töppel, C. Marquardt, E. Giacobino, and G. Leuchs, "Quantum-like nonseparable structures in optical beams," New J. Phys. **17**(4), 043024 (2015).
3. K. H. Kagalwala, G. Di Giuseppe, A. F. Abouraddy, and B. E. A. Saleh, "Bell's measure in classical optical coherence," Nat. Photonics **7**(1), 72–78 (2013).
4. A. N. de Oliveira, S. P. Walborn, and C. H. Monken, "Implementing the Deutsch algorithm with polarization and transverse spatial modes," J. Opt. B: Quantum Semiclassical Opt. **7**(9), 288–292 (2005).
5. B. Ndagano, B. Perez-Garcia, F. S. Roux, M. McLaren, C. Rosales-Guzman, Y. Zhang, O. Mouane, R. I. Hernandez-Aranda, T. Konrad, and A. Forbes, "Characterizing quantum channels with non-separable states of classical light," Nat. Phys. **13**(4), 397–402 (2017).
6. H. E. Kondakci and A. F. Abouraddy, "Diffraction-free space–time light sheets," Nat. Photonics **11**(11), 733–740 (2017).
7. S. Shabahang, H. E. Kondakci, M. L. Villinger, J. D. Perlstein, A. E. Halawany, and A. F. Abouraddy, "Omni-resonant optical micro-cavity," Sci. Rep. **7**(1), 10336 (2017).
8. F. Töppel, A. Aiello, C. Marquardt, E. Giacobino, and G. Leuchs, "Classical entanglement in polarization metrology," New J. Phys. **16**(7), 073019 (2014).
9. H. Rubinsztein-Dunlop, A. Forbes, M. V. Berry, M. R. Dennis, D. L. Andrews, M. Mansuripur, C. Denz, C. Alpmann, P. Banzer, T. Bauer, E. Karimi, L. Marrucci, M. Padgett, M. Ritsch-Marte, N. M. Litchinitser, N. P. Bigelow, C. Rosales-Guzmán, A. Belmonte, J. P. Torres, T. W. Neely, M. Baker, R. Gordon, A. B. Stilgoe, J. Romero, A. G. White, R. Fickler, A. E. Willner, G. Xie, B. McMorran, and A. M. Weiner, "Roadmap on structured light," J. Opt. **19**(1), 013001 (2017).
10. S. Berg-Johansen, F. Töppel, B. Stiller, P. Banzer, M. Ornigotti, E. Giacobino, G. Leuchs, A. Aiello, and C. Marquardt, "Classically entangled optical beams for high-speed kinematic sensing," Optica **2**(10), 864 (2015).
11. A. Ashkin, "Acceleration and trapping of particles by radiation pressure," Phys. Rev. Lett. **24**(4), 156–159 (1970).

Optics EXPRESS

12. A. Ashkin, J. M. Dziedzic, J. E. Bjorkholm, and S. Chu, "Observation of a single-beam gradient force optical trap for dielectric particles," Opt. Lett. **11**(5), 288–290 (1986).
13. S. Roy, K. Ushakova, Q. van den Berg, S. F. Pereira, and H. P. Urbach, "Radially Polarized Light for Detection and Nanolocalization of Dielectric Particles on a Planar Substrate," Phys. Rev. Lett. **114**(10), 103903 (2015).
14. A. Bag, M. Neugebauer, P. Woźniak, G. Leuchs, and P. Banzer, "Transverse Kerker Scattering for Angstrom Localization of Nanoparticles," Phys. Rev. Lett. **121**(19), 193902 (2018).
15. X. Zambrana-Puyalto, X. Vidal, P. Wozniak, P. Banzer, and G. Molina-Terriza, "Tailoring multipolar Mie scattering with helicity and angular momentum," ACS Photonics **5**(7), 2936–2944 (2018).
16. S. Nechayev, J. S. Eismann, M. Neugebauer, and P. Banzer, "Shaping Field Gradients for Nanolocalization," ACS Photonics **7**(3), 581–587 (2020).
17. B. Richards and E. Wolf, "Electromagnetic Diffraction in Optical Systems. II. Structure of the Image Field in an Aplanatic System," Proc. R. Soc. Lond. A **253**(1274), 358–379 (1959).
18. W. L. Erikson and S. Singh, "Polarization properties of Maxwell-Gaussian laser beams," Phys. Rev. E **49**(6), 5778–5786 (1994).
19. R. Dorn, S. Quabis, and G. Leuchs, "Sharper Focus for a Radially Polarized Light Beam," Phys. Rev. Lett. **91**(23), 233901 (2003).
20. L. Novotny and B. Hecht, Principles of Nano-Optics (Cambridge University Press, 2012).
21. A. Aiello and M. Ornigotti, "Near field of an oscillating electric dipole and cross-polarization of a collimated beam of light: Two sides of the same coin," Am. J. Phys. **82**(9), 860–868 (2014).
22. S. Yan and B. Yao, "Radiation forces of a highly focused radially polarized beam on spherical particles," Phys. Rev. A **76**(5), 053836 (2007).
23. T. A. Nieminen, N. R. Heckenberg, and H. Rubinsztein-Dunlop, "Forces in optical tweezers with radially and azimuthally polarized trapping beams," Opt. Lett. **33**(2), 122–124 (2008).
24. M. Michihata, T. Hayashi, and Y. Takaya, "Measurement of axial and transverse trapping stiffness of optical tweezers in air using a radially polarized beam," Appl. Opt. **48**(32), 6143 (2009).
25. Y. Kozawa and S. Sato, "Optical trapping of micrometer-sized dielectric particles by cylindrical vector beams," Opt. Express **18**(10), 10828–10833 (2010).
26. M. G. Donato, S. Vasi, R. Sayed, P. H. Jones, F. Bonaccorso, A. C. Ferrari, P. G. Gucciardi, and O. M. Maragó, "Optical trapping of nanotubes with cylindrical vector beams," Opt. Lett. **37**(16), 3381 (2012).
27. J.-B. Béguin, J. Laurat, X. Luan, A. P. Burgers, Z. Qin, and H. J. Kimble, "Reduced volume and reflection for optical tweezers with radial Laguerre-Gauss beams," Proc. Natl. Acad. Sci. U. S. A. **117**(42), 26109–26117 (2020).
28. K. Svoboda, C. F. Schmidt, B. J. Schnapp, and S. M. Block, "Direct observation of kinesin stepping by optical trapping interferometry," Nature **365**(6448), 721–727 (1993).
29. S. Bayoudh, T. A. Nieminen, N. R. Heckenberg, and H. Rubinsztein-Dunlop, "Orientation of biological cells using plane-polarized Gaussian beam optical tweezers," J. Mod. Opt. **50**(10), 1581–1590 (2003).
30. R. S. Dutra, N. B. Viana, P. A. M. Neto, and H. M. Nussenzveig, "Polarization effects in optical tweezers," J. Opt. B: Quantum Semiclassical Opt. **9**(8), S221–S227 (2007).
31. S. J. Parkin, R. Vogel, M. Persson, M. Funk, V. L. Loke, T. A. Nieminen, N. R. Heckenberg, and H. Rubinsztein-Dunlop, "Highly birefringent vaterite microspheres: production, characterization and applications for optical micromanipulation," Opt. Express **17**(24), 21944 (2009).
32. K. Visscher, S. P. Gross, and S. M. Block, "Construction of multiple-beam optical traps with nanometer-resolution position sensing," IEEE J. Sel. Top. Quantum Electron. **2**(4), 1066–1076 (1996).
33. T. Higuchi, Q. D. Pham, S. Hasegawa, and Y. Hayasaki, "Three-dimensional positioning of optically trapped nanoparticles," Appl. Opt. **50**(34), H183–H188 (2011).
34. M. Yevnin, D. Kasimov, Y. Gluckman, Y. Ebenstein, and Y. Roichman, "Independent and simultaneous three-dimensional optical trapping and imaging," Biomed. Opt. Express **4**(10), 2087 (2013).
35. P. Memmolo, L. Miccio, M. Paturzo, G. D. Caprio, G. Coppola, P. A. Netti, and P. Ferraro, "Recent advances in holographic 3D particle tracking," Adv. Opt. Photonics **7**(4), 713 (2015).
36. J. S. Batchelder and M. A. Taubenblatt, "Interferometric detection of forward scattered light from small particles," Appl. Phys. Lett. **55**(3), 215–217 (1989).
37. A. Pralle, M. Prummer, E.-L. Florin, E. H. K. Stelzer, and J. K. H. Hörber, "Three-dimensional high-resolution particle tracking for optical tweezers by forward scattered light," Microsc. Res. Tech. **44**(5), 378–386 (1999).
38. A. Rohrbach and E. H. K. Stelzer, "Three-dimensional position detection of optically trapped dielectric particles," J. Appl. Phys. **91**(8), 5474–5488 (2002).
39. A. Rohrbach, H. Kress, and E. H. Stelzer, "Three-dimensional tracking of small spheres in focused laser beams: influence of the detection angular aperture," Opt. Lett. **28**(6), 411–413 (2003).
40. S. F. Tolić-Nørrelykke, E. Schäffer, J. Howard, F. S. Pavone, F. Jülicher, and H. Flyvbjerg, "Calibration of optical tweezers with positional detection in the back focal plane," Rev. Sci. Instrum. **77**(10), 103101 (2006).
41. J. Hwang and W. Moerner, "Interferometry of a single nanoparticle using the Gouy phase of a focused laser beam," Opt. Commun. **280**(2), 487–491 (2007).
42. L. Friedrich and A. Rohrbach, "Tuning the detection sensitivity: a model for axial backfocal plane interferometric tracking," Opt. Lett. **37**(11), 2109 (2012).

Optics EXPRESS

43. F. Tebbenjohanns, M. Frimmer, and L. Novotny, "Optimal position detection of a dipolar scatterer in a focused field," Phys. Rev. A **100**(4), 043821 (2019).
44. P. Debye, "Das Verhalten von Lichtwellen in der Nähe eines Brennpunktes oder einer Brennlinie," Ann. Phys. **335**(14), 755–776 (1909).
45. A. Beckley, T. G. Brown, and M. A. Alonso, "Full Poincaré Beams," Opt. Express **18**(10), 10777–10785 (2010).
46. T. Staudt, M. C. Lang, R. Medda, J. Engelhardt, and S. W. Hell, "2, 2'-Thiodiethanol: A new water soluble mounting medium for high resolution optical microscopy," Microsc. Res. Tech. **70**(1), 1–9 (2007).
47. P. Banzer, M. Neugebauer, A. Aiello, C. Marquardt, N. Lindlein, T. Bauer, and G. Leuchs, "The photonic wheel - demonstration of a state of light with purely transverse angular momentum," J. Eur. Opt. Soc.-Rapid **8**, 13032 (2013).